

Optical Properties in The Hole-Doped $\text{Ca}_{8.5}\text{Na}_{1.5}(\text{Pt}_3\text{As}_8)(\text{Fe}_2\text{As}_2)_5$ Single Crystal

W. J. Choi

Daegu Gyeongbuk Institute of Science and Technology

Y. I. Seo

Daegu Gyeongbuk Institute of Science and Technology

Shin-ichi Kimura

Osaka University

Yong Seung Kwon (✉ yskwon@dgist.ac.kr)

Daegu Gyeongbuk Institute of Science and Technology

Research Article

Keywords: strong correlation effect, Hund's coupling, high-frequency spectral weight transfer, superconducting gap, pseudogap, hole-doped $(\text{Ca}_{1-x}\text{Na}_x)_{10}(\text{Pt}_3\text{As}_8)(\text{Fe}_2\text{As}_2)_5$

Posted Date: March 3rd, 2021

DOI: <https://doi.org/10.21203/rs.3.rs-257280/v1>

License:  This work is licensed under a Creative Commons Attribution 4.0 International License.

[Read Full License](#)

Version of Record: A version of this preprint was published at Results in Physics on August 1st, 2021. See the published version at <https://doi.org/10.1016/j.rinp.2021.104468>.

Optical properties in the hole-doped $\text{Ca}_{8.5}\text{Na}_{1.5}(\text{Pt}_3\text{As}_8)(\text{Fe}_2\text{As}_2)_5$ single crystal

W. J. Choi^{1,†}, Y. I. Seo^{1,†}, Shin-ichi Kimura^{2,3} and Yong Seung Kwon^{1,*}

¹Department of Emerging Materials Science, DGIST, Daegu 711-873, Republic of Korea

²Graduate School of Frontier Biosciences and Department of Physics, Graduate School of Science, Osaka University, Suita 565-0871, Japan

³Institute for Molecular Science, Okazaki 444-8585, Japan

For newly synthesized hole-doped $\text{Ca}_{8.5}\text{Na}_{1.5}(\text{Pt}_3\text{As}_8)(\text{Fe}_2\text{As}_2)_5$ single crystals, we measured the infrared reflectivity spectrum and the magnetic field dependence of magnetoresistivity and Hall resistivity. The results of these two experiments in normal states are well described by two band models. In the normal state below 150 K, the optical conductivity spectrum shows a transfer of spectral weights from the mid-infrared region to the near-infrared region. Meanwhile, the magnetoresistance and Hall resistance show a significant decrease in carrier density at 150 K. These two phenomena are due to the conversion of itinerant electrons to heavy electrons by the strong correlation effect, Hund's coupling. In the superconducting state, the spectral weight in the low frequency region by the superconducting condensate is completely suppressed, which is well analyzed by the generalized Mattis-Bardeen (M-B) model with a two superconducting gap.

Keywords: strong correlation effect, Hund's coupling, high-frequency spectral weight transfer, superconducting gap, pseudogap, hole-doped $(\text{Ca}_{1-x}\text{Na}_x)_{10}(\text{Pt}_3\text{As}_8)(\text{Fe}_2\text{As}_2)_5$

* Corresponding author

E-mail address: ykwon@dgist.ac.kr (Yong Seung Kwon)

† Equally contributing authors

Introduction

The recently discovered superconducting $\text{Ca}_{10}(\text{Pt}_3\text{As}_8)(\text{Fe}_2\text{As}_2)_5$ (herein called Ca10-3-8) has been added to another new family of iron-based superconductors¹⁻³. This superconductor exhibits the behavior of a prototype between the subtle competition and coexistence of magnetism and superconductivity found in other iron-based superconductors. This compound shows a stacked crystal structure of a Ca-(Pt₃As₈)-Ca-(Fe₂As₂) layer, where the Ca layer serves as a reservoir layer that supplies electric charges to the Fe₂As₂ layer, and the Pt₃As₈ layer serves as an intermediate layer controlling the distance between the Fe₂As₂ layers¹. This crystal structure is similar to the oxide superconductor $\text{Bi}_2\text{Sr}_2\text{Ca}_{n-1}\text{Cu}_n\text{O}_{2n+4+x}$ (BSCCO) with an intermediate layer⁴. This BSCCO superconductor is an interesting material that provides a relationship between the superconducting coupling between the superconducting layers, which is controlled by an interlayer inserted between the superconducting CuO₂ layers, and the strengthening of the superconducting temperature⁵⁻⁷. In this context, our material is one of the few candidates to study T_c enhancement in iron-based superconductors, and thus has attracted much attention in the field of superconductivity.

The Ca10-3-8 parent compound, unlike other typical FeAs superconductors, is semiconducting and antiferromagnetically ordered without any further reduction in crystal symmetry at $T_N \sim 110$ K. The doping effect in the parent compound leads to superconductivity⁸. Electron doping effect occurs when La is replaced at Ca site and Pt is substituted at Fe site, and hole doping effect can occur when Na is substituted at Ca site. For electron-doped compounds by La or Pt substitution, the maximum T_c is 35 and 13 K, respectively^{9,10}. Meanwhile, hole doping compounds have not been reported so far. The parent compound has multiple Fermi surfaces like other typical FeAs-superconductors, and the subtle differences of this Fermi surface induce superconductivity at $T_c = 8$ K without doping¹¹.

To study the delicate relationship between electronic structure and superconductivity, various experiments such as transport^{1,12}, ARPES^{11,13}, upper critical field^{10,12,14}, thermally activated vortex pinning¹⁵, pressure effect¹⁶, penetration depth^{17,18}, infrared spectroscopy experiments¹⁹⁻²¹, etc. have already been performed in the Ca10-3-8 family. In particular, the infrared spectroscopy experiment was

recently performed on La-doped Ca10-3-8, electron-doped, by Seo et al., and the multi-band effect, superconducting gap structure, pseudo gap structure above T_c , and spectral weight transfer to high frequency were observed^{19,20}. The multi-band effect was understood as the Drude-Lorentz model, the superconducting gap structure as a generalized Mattis-Bardeen model with two superconducting gaps, and the pseudo gap structure as a preformed Cooper pairs model. However, in his study, it was suggested that the spectral weight transfer to a high frequency is related to a strong correlation effect such as Hubbard interaction or Hund's coupling. It is very interesting whether this transfer of spectral weights can be observed even in a hole doping system. According to the previously reported results, the spectral weight transfer was observed in the electron doping system where Co was substituted for the Fe site in Ba122, but the transfer was weakened in the optimally hole-doping system replaced with K in the Ba site, and the transfer completely disappeared in pure KFe_2As_2 ²².

From this point of view, optical studies in Na-doped Ca10-3-8, hole-doped, material treated in this study are very suitable candidates to solve the important problem for this spectral weight transfer. Interestingly, we clearly observed the transfer of the spectral weights from the mid-infrared region to the near-infrared region below about 150 K in the infrared spectrum experiment for Na-doped Ca10-3-8 material. It could be concluded that the transfer was not related to the Hubbard interaction due to the discovery of a continuous temperature dependence of the weights of the optical spectrum in the low frequency region. We applied Hund's coupling to understand the transfer of this spectral weight, which well explained the decrease in the itinerant electron density evaluated by the Hall resistivity and magnetoresistivity occurring below 150 K. Combined with previous reports on observations of spectral weight transfers to high frequency regions in several FeAs superconductors, our observations clearly indicate that the transfer of spectral weights to high frequency regions above 0.5 eV is caused by the Hund's coupling effect.

Results and discussion

The X-ray diffraction patterns of a hole-doped $\text{Ca}_{8.5}\text{Na}_{1.5}(\text{Pt}_3\text{As}_8)(\text{Fe}_2\text{As}_2)_5$ single crystal, which has

not been reported so far, is shown in Fig. 1. Only (00*l*) peaks were observed, which indicates that this single crystal is well aligned in the (00*l*) direction. The full width at half maximum (FWHM) of the (002) peak is very small as 0.08°, indicating the high-quality single crystal. The (00*l*) diffraction patterns were analysed using the UNITCELL software²³ to obtain the interlayer distance d_{FeAs} of the FeAs layers. The evaluated d_{FeAs} is 10.538 Å, which is large compared to the parent ($d_{\text{FeAs}} = 10.31$ Å) and optimally La-doped 1038 ($d_{\text{FeAs}} = 10.35$ Å)¹². Since the ionic radius of Na⁺ is slightly smaller, 99%, than that of La³⁺, the interplanar distance d_{FeAs} of Ca_{8.5}Na_{1.5}(Pt₃As₈)(Fe₂As₂)₅ is expected to be slightly smaller or almost the same, but d_{FeAs} in the hole-doped Ca_{8.5}Na_{1.5}(Pt₃As₈)(Fe₂As₂)₅ is about 2 % larger than d_{FeAs} in the electron-doped Ca_{8.5}La_{1.5}(Pt₃As₈)(Fe₂As₂)₅. This strongly suggests that the angle (∠) of As-Fe-As in Ca_{8.5}Na_{1.5}(Pt₃As₈)(Fe₂As₂)₅ is reduced compared to Ca_{8.5}La_{1.5}(Pt₃As₈)(Fe₂As₂)₅ because Na-doping instead of La-doping is not expected to induce a detectable change in Fe-As bond length.

Fig. 2 shows the temperature dependence of the electrical resistivity for a hole-doped Ca_{8.5}Na_{1.5}(Pt₃As₈)(Fe₂As₂)₅ single crystal. The electrical resistivity shows zero at low temperatures due to its superconductivity, increases abruptly at 35.5 K, and then increases slowly in the normal state. If the temperature at half of the normal state electrical resistivity is defined as the superconducting transition temperature, the superconducting critical temperature is estimated as $T_c = 36.3$ K. From the criterion of superconducting transition width $\Delta T_c = 2 \cdot (T_c - T_{c, \text{zero}})$, ΔT_c is estimated to be 1.6 K, which is narrow, indicating a good-quality single crystal. Interestingly, a weak inflection point exists at $T_{\text{ps}} = 110$ K in the temperature dependence curve of electrical resistivity; as shown in the inset of Fig. 2, a weak peak or shoulder in the first-order differential of the resistivity to temperature, $d\rho(T)/dT$, and a crossover from positive to negative in the second-order differential of resistivity, $d^2\rho(T)/dT^2$, were observed at T_{ps} . Such an inflection point was observed when the pseudogap was opened in high- T_c cuprates²⁴ and FeSe²⁵, indicating that the pseudogap opening occurs at a part of the Fermi surfaces also in Ca_{8.5}Na_{1.5}(Pt₃As₈)(Fe₂As₂)₅ at T_{ps} .

Fig. 3 shows the frequency dependence of the reflectivity $R(\omega)$ measured in the Ca_{8.5}Na_{1.5}(Pt₃As₈)(Fe₂As₂)₅ single crystal at several temperatures on a semi-logarithmic scale. In the

normal state, the reflectivity $R(\omega)$ in the low frequency region approaches unity as the frequency decreases down to zero, and the approach becomes faster as the temperature decreases, which is due to the metallic properties of $\text{Ca}_{8.5}\text{Na}_{1.5}(\text{Pt}_3\text{As}_8)(\text{Fe}_2\text{As}_2)_5$ according to the Drude model. The peak structures due to interband transitions are observed in the high-frequency region near 4500 cm^{-1} . The frequency corresponding to the peak location is much higher than the measured temperature, but the peak exhibits a significant temperature dependence. Below about 4500 cm^{-1} , the reflectivity is almost unchanged in the higher temperature range than 150 K and decreases significantly in the lower temperature range. At about 4500 cm^{-1} , as seen in the inset in Fig. 3, the reflectivity spectra of the two temperature groups intersect, then the magnitude of the reflectivity of the two groups is inverted. In the whole temperature range from normal state to superconducting state, each reflectivity spectrum clearly shows an abnormal peak structure due to the interband transition along with the Drude reflection of the intraband transition in the intermediate frequency range of 200 to 1500 cm^{-1} . Below the T_{ps} , the reflectivity spectrum shows another anomaly like hump at around 100 cm^{-1} and it disappears below T_c . At 8 K, superconducting state, the reflectivity spectrum increases sharply below 300 cm^{-1} compared to the normal state's reflectivity spectrum and then reaches unity at about 90 cm^{-1} , which reflects the opening of the s-wave-like superconducting gap. A similar reflectivity spectrum was observed at 20 K, which is still superconducting, but the region of the unity reflectivity was reduced down to 70 cm^{-1} .

To further investigate the temperature dependence of the reflectivity spectrum, the frequency dependent optical conductivity $\sigma_1(\omega)$ was derived by the Kramers-Kronig (K-K) transformation to the measured reflectivity data, which is shown in Fig. 4. A sharp feature in the conductivity is observed at around 230 cm^{-1} , which is attributed to infrared-active lattice vibrations. In the normal state, $\sigma_1(\omega)$ in the frequency region below 1500 cm^{-1} consists of two narrow peaks at around 300 and 700 cm^{-1} along with a pronounced Drude response over the entire region. The Drude response shows a peak centered at $\omega = 0$, and as temperature decreases, the peak narrows in width and increases in height, indicating the development of coherence. On the other hand, the two peaks observed at about 300 and 700 cm^{-1} are independent of temperature for the peak position, but show temperature dependence for their width and height, i.e. as the temperature increases, the width (height) of the peaks increases (decreases). This

behavior is the typical temperature dependence of the optical spectrum for narrow interband transitions. Even in the superconducting state, the peaks are observed. A peak with the similar temperature dependence was observed in the La-underdoped Ca10-3-8 sample, but the peak width is slightly large, especially the peak at 700 cm^{-1} . However, it was not observed in the optimal La-doped Ca10-3-8 sample, probably because the peaks were broadened. According to the band calculation of parent $\text{Ca}_{10}(\text{Pt}_3\text{As}_8)(\text{Fe}_2\text{As}_2)_5^{11}$, the peaks in the low-frequency region are mainly due to the transition of a part of Fe-3d electrons onto Fermi energy. Due to multiple orbitals of Fe-3d electrons, the 3d electrons may have been itinerant or localized. The peaks observed near 300 and 700 cm^{-1} are caused by localized 3d orbitals because the width of the peaks is very narrow.

Interestingly, a strong temperature dependence of optical conductivity was observed in the high frequency region from the mid-infrared, mainly composed of intraband transitions, to the near-infrared region, mainly composed of interband transitions. The temperature dependence characteristics are as follows: In the frequency range below 5000 cm^{-1} , the optical conductivity spectrum shows a very weak temperature dependence in the temperature range of 300 to 150 K , decreases significantly when the temperature decreases from 150 to 100 K , then slowly decreases again below 100 K . On the other hand, in the frequency range above 5000 cm^{-1} , the temperature dependence of optical conductivity shows the opposite behavior to that in the region below 5000 cm^{-1} described above; In other words, the optical conductivity increases very slowly up to 100 K , then suddenly increases significantly from 100 to 150 K , and hardly changes above 150 K . In the superconducting state, the optical conductivity in the range below 5000 cm^{-1} has almost no temperature dependence below 50 K . However, in the range above 5000 cm^{-1} , the optical conductivity spectral intensity gradually decreases as the temperature decreases compared to that at 50 K .

The optical conductivity in the normal temperature range from T_{ps} to T_c shows a peak around 80 cm^{-1} along with the Drude response. When the temperature was lowered, the location of the peak seems to be almost temperature independent, and the width was clearly widened and the height decreased. This peak disappears in the superconducting state. Similar peaks were also observed in the La-doped

sample¹⁹. According to this report, from a phenomenological approach using the preformed Cooper pair model²⁶, it was confirmed that this peak was due to pseudogap formation. The temperature at which the pseudogap peak was observed in the sample of this study is almost similar to the pseudogap formation temperature in electrical resistivity. In the superconducting state, at 8 K, the optical conductivity began to be suppressed below about 200 cm⁻¹ and was completely suppressed below 90 cm⁻¹. When the temperature rises, the suppression of optical conductivity occurs slowly and becomes complete below 70 cm⁻¹. The suppression of this optical conductivity is caused by superconducting condensates resulting from the formation of Cooper pairs. The complete suppression of the optical conductivity indicates the formation of a nodeless s-wave superconducting gap. The frequency of this complete suppression is approximately equal to the energy scale of the pseudogap peak.

To quantitatively analyze the optical conductivity in the normal state, we attempted to fit the optical conductivity in normal states with a Lorentz-Drude (L-D) model:

$$\sigma(\omega) = \frac{1}{4\pi} \text{Re} \left[\sum_k S_k \frac{\omega}{\tau_{Lk} + i(\omega_{Lk}^2 - \omega^2)} + \sum_j \frac{\Omega_{Pj}^2}{\tau_{Dj} - i\omega} \right], \quad (2)$$

where S_k , ω_{Lk} and $1/\tau_{Lk}$ are the oscillator strength, Lorentz oscillator frequency, and scattering rate of the k th oscillator, respectively, while Ω_{Pj} and $1/\tau_{Dj}$ are the plasma frequency and scattering rate for the j th free carrier Drude band, respectively. The fitting using this L-D model is performed in the temperature region above the T_{ps} where no pseudogap is found in the normal state. The reason for choosing the temperature range above the T_{ps} in this fitting is that the excitation spectrum of the pseudogap cannot simply be treated as a Lorentzian without a theoretical approach. Fig. 5 shows the fitting result for the optical conductivity at 150 K as a representative. The optical conductivity spectrum at 150 K is well represented by the eight Lorentz oscillator components and two Drude components. The parameters of the eight Lorentz oscillator components are listed in Table 1. The resonance frequencies for most Lorentz oscillators used in the fitting are almost similar to those in the normal state

for La-underdoped Ca10-3-8²⁰. However, the peaks around 200 and 700 cm⁻¹ in the hole-doped Ca_{8.5}Na_{1.5}(Pt₃As₈)(Fe₂As₂)₅ sample appear clearly with a narrower width than those in La-underdoped Ca1038 sample, which may be due to the narrowing of the Fe-3*d* electron band mentioned above. The two Drude components in the fitting indicate the presence of multiple bands, as in many IBS compounds²⁷⁻³². The temperature dependences of the plasma frequency and scattering rate of each band are shown in Figs. 6a and b, respectively. One band is a broad band with a large scattering rate and plasma frequency, and the other is a narrow band with a fairly small scattering rate and plasma frequency. The two plasma frequencies are independent of temperature from 300 down to 150 K, but the two scattering rates decrease almost linearly as the temperature decreases. Fig. 6c shows the d. c. conductivity σ_{dc} , calculated from the plasma frequency and the scattering rate of each band, at $\omega = 0$. In the figure, $\sigma_{dc,1}$ and $\sigma_{dc,2}$ are for the broad Drude band and narrow Drude band, respectively. The sum of $\sigma_{dc,1}$ and $\sigma_{dc,2}$ agrees well with σ_{dc} measured by the electrical resistivity method over the entire temperature range, indicating that the parameters obtained from the fitting are reasonable. As shown in the figure, $\sigma_{dc,1}$ is significantly large compared to $\sigma_{dc,2}$, indicating that the electrical transport in Ca_{8.5}Na_{1.5}(Pt₃As₈)(Fe₂As₂)₅ is dominated by carriers belonging to the broad Drude band.

In order to understand the temperature dependence of the spectral weight transfer mentioned above, calculation of the spectral weight is required. The spectral weight at each temperature normalized to the spectral weight at 300 K is defined as

$$SW(T; \omega_c) = \int_{0^+}^{\omega_c} \sigma_1(T; \omega) / \sigma_1(300 \text{ K}; \omega) d\omega, \quad (1)$$

where ω_c is the cutoff frequency. SW calculated at each temperature for $\omega_c \geq 1000 \text{ cm}^{-1}$ and $\omega_c \leq 1000 \text{ cm}^{-1}$ are shown in Figs. 7a and b, respectively. As shown in Fig. 7a, SW at $\omega_c = 10000 \text{ cm}^{-1}$ shows almost 1 from 300 K down to T_c , which indicates that the sum rule is satisfied at $\omega_c = 10000 \text{ cm}^{-1}$, that is, the spectral weight up to 10000 cm⁻¹ is conserved for temperature changes. This was also observed in La-doped Ca10-3-8 reported previously¹⁹. In $1000 < \omega_c < 10000 \text{ cm}^{-1}$, SW decreases as the temperature decreases in the normal state. A decrease in SW from 1 at any ω_c means that the spectral weight is transferred from the frequency region below ω_c to the region above it. The reduction in SW is not

simple; SW hardly changes up to 150 K, then abruptly decreases below that temperature. The rate of decrease in SW below 150 K does not increase monotonically as ω_c decreases; As ω_c decreases from 10000 cm^{-1} , the decrease rate increases and reaches a maximum at $\omega_c = 4000 \text{ cm}^{-1}$ and then ω_c decreases to 2000 cm^{-1} . At $\omega_c = 1000 \text{ cm}^{-1}$, SW becomes almost constant again to 1 in the normal state, i.e., SW at $\omega_c = 1000 \text{ cm}^{-1}$ is partially conserved and the partial sum rule is recovered. Fig. 7b shows a similar plot of SW for $\omega_c < 1000 \text{ cm}^{-1}$. The temperature dependence of SW at $\omega_c < 1000 \text{ cm}^{-1}$ shows the opposite temperature dependence of that at $\omega_c > 1000 \text{ cm}^{-1}$ shown in Fig. 7a, that is, SW at $\omega_c < 1000 \text{ cm}^{-1}$ increases as the temperature decreases. Increasing SW from 1 at any ω_c means that the spectral weight has been transferred from the frequency region above ω_c to the region below it. The SW increases monotonically as the temperature decreases from 300 K. The rate of increase increases as ω_c decreases. The large reduction in SW below T_c is due to the superconducting condensate.

The transfer of spectral weight showing such complicated temperature dependence is roughly divided into two parts: one part below $\omega_m = 1000 \text{ cm}^{-1}$ and the other part above ω_m . Each part separately conserves the spectral weight above T_c . To understand this, we look back on the optical conductivity data in Fig. 4, where a large fraction of the optical spectra in the intermediate frequency range of 700-5000 cm^{-1} is undetermined at high temperatures and hence remains incoherent. As the temperature decreases, the incoherence spectra gradually turn into coherent spectra. At the same time, the incoherence spectra were reduced due to the transfer to the low frequency Drude region or the high frequency Lorentz region. The transfer to the low frequency Drude region is well understood by the sharpening of the Drude spectrum due to the development of coherent quasiparticles, whereas the transfer to the high frequency interband transition region, which is more apparent below 150 K, is reported to be associated with heavy itinerant electrons due to strong correlation effects of the local interactions, such as the Hubbard interaction and Hund's coupling^{22,33}.

The Hubbard interaction reconstructs the band at low temperature so that the optical conductivity in the intermediate frequency region is transferred to the low frequency Drude region as well as the high frequency interband transition region. As can be seen in Fig. 7a, the relative spectral weight for

$\omega_c < 10000 \text{ cm}^{-1}$ has a value less than 1 below $\sim 150 \text{ K}$. This indicates that the spectral weight is transferred from the middle frequency region to the high frequency region below $\sim 150 \text{ K}$, considering that the relative spectral weight is conserved at $\omega_c = 10000 \text{ cm}^{-1}$. Assuming this transfer is due to the Hubbard interaction, it indicates that the interaction works effectively at temperatures below about 150 K . Then, the SW at $\omega_c < 1000 \text{ cm}^{-1}$ should show an abrupt increase around 150 K in addition to a continuous increase due to the development of coherent quasiparticles as the temperature decreases. However, as shown in Fig. 7b, the relative spectral weight only increases continuously as the temperature decreases. Therefore, the transfer of spectral weights into the high frequency region is not due to the Hubbard interaction effect.

On the other hand, the Hund's coupling energy between localized magnetic moments and itinerant electrons is known to be approximately 0.6 eV in iron-based superconductors²². Hund's coupling is highly dependent on temperature, depending on the degree of localization of the magnetic moment and the degree to which the magnetic moment approaches the Fermi energy. In other words, the magnetic moment is localized below the characteristic temperature (T_{Hund}) and causes the Hund's coupling with itinerant electrons, but at higher temperatures, the magnetic moment is thermally excited and loses localization and does not cause the Hund's coupling. In the temperature range below T_{Hund} , the itinerant electrons become heavier and lose their role as the itinerant electrons, and behave like electrons bound by the magnitude of the Hund coupling energy. Therefore, below T_{Hund} , the optical conductivity spectrum is transferred from the middle frequency region to the frequency region as high as about 0.6 eV . As shown in Fig. 7b, the relative spectral weight less than 1 in the temperature region below 150 K and the change with ω_c in the above-described spectral weight reduction rate indicate that the spectral weight is transferred from the intermediated frequency region to the frequency region above 5000 cm^{-1} . This is in good agreement with the results of Hund's coupling. T_{Hund} in $\text{Ca}_{8.5}\text{Na}_{1.5}(\text{Pt}_3\text{As}_8)(\text{Fe}_2\text{As}_2)_5$ is equivalent to about 150 K . The Hund's coupling does not affect the lower frequency spectrum due to intraband transitions, which also agrees well with our data.

The generation of heavy electrons by Hund' coupling below 150 K reduces the density of the

itinerant electrons. So, the observation of carrier density reduction below T_{Hund} will give direct evidence of Hund's coupling. The evaluation of carrier reduction below T_{Hund} can be performed by fitting using the L-D model for optical conductivity. However, as discussed above, fitting of optical conductivity using the L-D model is currently impossible due to the presence of pseudogap below T_{Hund} . Instead, to confirm this, the magnetic field dependence on the Hall resistivity and the magnetoresistivity was measured at various temperatures. By applying the two carrier models to these two experimental results, we evaluated the concentration and mobility of the carrier. The application of these two carrier models is based on the analysis of optical conductivity in the normal state discussed above. The concentration and mobility of each carrier evaluated by both data are shown in Figs. 8a and b, respectively. For more information on this evaluating method, refer to Supplementary Information. As shown in the figure, the carrier density and mobility evaluated by the magnetoresistivity and Hall resistivity differ by about 3% in the high temperature region, which is within error. The low carrier density is about $8 \times 10^{18} \text{ cm}^{-3}$ and is temperature independent. The high carrier density is almost constant at about $1.9 \times 10^{21} \text{ cm}^{-3}$ in the high temperature region, then begins to decrease at 150 K and approaches $1.5 \times 10^{21} \text{ cm}^{-3}$ below 100 K. For carriers with high density, a reduction of about 15% was observed below 150 K. This reduction strongly supports the conversion of itinerant electrons to heavy electrons by Hund's coupling, as discussed above. Therefore, it was more clearly demonstrated that the transfer of the spectral weights in the middle frequency range to the high frequency range below 150 K was due to Hund's coupling. The mobility of both carriers increases as the temperature decreases. This is due to the developed coherence of carriers. However, the mobility of carriers with a high density increases significantly below 150 K. This is due to a decrease in the density of carriers with a high density at that temperature. The effective mass m^* obtained by combining the plasma frequency evaluated by optical measurement and the carrier density measured by electrical transport is estimated as $1.5m_0$ for high carrier density and $1.0m_0$ for low carrier density. Hund's coupling, a ferromagnetic interaction between itinerant electrons and localized electrons, ferromagnetically induces magnetic order. However, as in the temperature dependence of the electrical resistivity in Fig. 2, no anomaly in electrical resistivity due to magnetic order was observed. This means that this Hund's coupling only leads to short-range order.

As shown in Fig. 4, the optical conductivity $\sigma_1(\omega)$ at 8 and 20 K, the superconducting state, is completely suppressed to zero at about 90 and 70 cm^{-1} , respectively, due to the opening of the s-wave superconducting energy gap. Since the optical conductivity and electrical transport results in the normal state discussed above are well explained by two-carrier model, it would be reasonable to think that the opening of two s-wave superconducting gaps occurs in the superconducting state. Therefore, we used a generalized Mattis-Bardeen (M-B) model³⁴ with two superconducting gaps to fit the optical conductivity spectrum at 8 K. To obtain the excitation spectrum only by the superconducting gap open, the optical conductivity at 8 K eliminates the interband transition spectrum obtained by fitting at 150 K using the L-D model. The excitation spectrum due to the opening of the superconducting gap is shown in Fig. 9. As shown in the figure, the optical conductivity at 8 K shows good agreement with the results calculated from the M-B model with two superconducting energy gaps. From this fitting, the superconducting gap (Δ_i), the plasma frequency ($\Omega_{p_i}^{sn}$) and the scattering rates ($1/\tau_i^{sn}$) for the normal state band causing the superconducting gap are determined to be $\Delta_1 = 41.9 \text{ cm}^{-1}$ (5.2 meV), $\Omega_{p_1}^{sn} = 8643 \text{ cm}^{-1}$ and $1/\tau_1^{sn} = 400 \text{ cm}^{-1}$ for the first band and $\Delta_2 = 54.8 \text{ cm}^{-1}$ (6.8 meV), $\Omega_{p_2}^{sn} = 4842 \text{ cm}^{-1}$ and $1/\tau_2^{sn} = 400 \text{ cm}^{-1}$ for the second band. The former superconducting energy gap appears to arise from a broad Drude band with a high plasma frequency (Ω_{p_1}) in normal state, and the latter superconducting energy gap appears to have arisen from a narrow Drude band with a low plasma frequency (Ω_{p_2}) in normal state, because the normal component plasma frequency ($\Omega_{p_1}^{sn}$) for the former gap is significantly larger than that ($\Omega_{p_2}^{sn}$) for the latter. However, $\Omega_{p_1}^{sn}$ corresponds to about 80% of the plasma frequency (Ω_{p_1}) for the broad Drude band in high temperature normal states, and $\Omega_{p_2}^{sn}$ is about 6 times larger than the plasma frequency (Ω_{p_1}) in normal state for a narrow Drude band. The causes of this difference will be discussed again below. On the other hand, the scattering rate ($1/\tau_1^{sn}$) for the former band is about the same as the scattering rate ($1/\tau_{D_1}$) for the broad Druder band in high temperature normal state, while the scattering rate ($1/\tau_2^{sn}$) for the latter band is very different from the scattering rate ($1/\tau_{D_2}$) of the narrow Drude band in normal state. These results can be clearly stated that the small superconducting energy gap is not formed in the narrow Drude band below T_c . The two scattering rates, $1/\tau_{D_1}^{sn}$ and $1/\tau_{D_2}^{sn}$, obtained in the superconducting state are equal to each other,

which is similar to the scattering rate ($1/\tau_{D1}$) of the broad Drude band in the high temperature normal state. Moreover, the sum of the carrier concentrations for the two normal component bands in the superconducting state is similar to that of the broad Drude band in the normal state, because the magnitude of $(\Omega_{P1}^{sn})^2 + (\Omega_{P2}^{sn})^2$ is almost same as that of $(\Omega_{P1})^2$. These results indicate that the two types of superconducting gaps obtained by fitting above are derived from the same broad Drude band obtained in the normal state, which may physically mean that an anisotropic superconducting gap with nodes was formed in the broad Drude band. However, the anisotropic superconducting gap with the node does not completely suppress the optical conductivity in the low frequency region and leaves a weak Drude response³⁵. This is completely different from our results. Another reason can be thought of in terms of infrared spectroscopy. In a multi-band system, if the scattering rates for different bands are the same, the optical conductivity obtained by infrared spectroscopy is not distinguished by different band, but represents the sum of the optical conductivity of different bands. According to this, the formation of two different magnitude superconducting gaps below T_c mentioned above indicates that the broad band is composed of two Drude bands with the same scattering rate.

Since $1/\tau_{1,2}^{sn} > 2\Delta_{1,2}$ for both bands, both superconducting gaps are in the dirty limit. The ratios of superconducting gap magnitude to T_c , $R = 2\Delta/k_B T_c$, were evaluated as 3.4 for small superconducting gap and 4.5 for large superconducting gap. Compared to $R_{BCS} = 3.5$ by the BCS theory²⁹, the mixed values of R suggest that the superconductivity in $\text{Ca}_{8.5}\text{Na}_{1.5}(\text{Pt}_3\text{As}_8)(\text{Fe}_2\text{As}_2)_5$ could be a mixture of weak-coupling and strong-coupling superconducting states. The gap values of $\text{Ca}_{8.5}\text{Na}_{1.5}(\text{Pt}_3\text{As}_8)(\text{Fe}_2\text{As}_2)_5$ are similar to the gap values of typical FeAs-SC compounds with similar T_c , e.g., $\text{Ca}_{8.5}\text{La}_{1.5}(\text{Pt}_3\text{As}_8)(\text{Fe}_2\text{As}_2)_5$ ($T_c = 35.2$ K; $\Delta_1 \approx 4.9$ meV, $\Delta_2 \approx 14.2$ meV)¹⁹ and $\text{Ba}_{0.6}\text{K}_{0.4}\text{Fe}_2\text{As}_2$ ($T_c = 37$ K; $\Delta_1 \approx 6$ meV, $\Delta_2 \approx 12$ meV)³⁶.

Conclusion

In summary, we measured the reflectivity spectrum from 8 to 300 K in the hole-doped $\text{Ca}_{8.5}\text{Na}_{1.5}(\text{Pt}_3\text{As}_8)(\text{Fe}_2\text{As}_2)_5$ single crystal ($T_c = 36.3$ K), and also measured the magnetic field

dependence of its magnetoresistivity and Hall resistivity. In the normal state, optical conductivity is well-fitted by the L-D model with two Drude responses and eight Lorentzian oscillators, and conductivity tensors $\sigma_{xx}(B)$ and $\sigma_{xy}(B)$ are well-fitted using a two-band model. The evaluated carrier density is constant at high temperatures and then decreases below 150 K. This is due to the decrease in the itinerant electron density due to Hund's coupling occurring below 150K. The decrease in the itinerant electron density leads to a transfer of spectral weights from the mid-infrared region to the near-infrared region in the optical conductivity spectrum.

In the superconducting state, the optical conductivity spectrum shows clean gap opening at about 80 cm^{-1} at 8 K. The optical conductivity fits well with two clean superconducting gaps, $\Delta_1 = 5.2 \text{ meV}$ and $\Delta_2 = 6.8 \text{ meV}$, which occur in the band with a large plasma frequency obtained with the L-D model in the normal state.

Methods

The $\text{Ca}_{8.5}\text{Na}_{1.5}(\text{Pt}_3\text{As}_8)(\text{Fe}_2\text{As}_2)$ single crystal was grown by the Bridgman method. We synthesized CaAs, NaAs, and FeAs precursors in evacuated quartz ampoules in advance at 550, 250, and 1050 °C, respectively. We mixed the resulting powders well in the mortar, and we put them in a clean BN crucible and then in a clean Mo crucible. The BN crucible was used to avoid chemical reaction between the Mo crucible and the Fe element. We then welded the Mo crucible and the Mo lid with an arc welder, which was done to prevent volatile arsenic defects at high temperatures. The welded Mo crucible was placed in a high-vacuum electric furnace having a high temperature stability of $\pm 0.1 \text{ }^\circ\text{C}$ and a single crystal was grown at 1250 °C. The single crystal obtained by this method has a size of $\sim 2 \times 2 \times 0.5 \text{ mm}^3$.

The X-ray diffraction experiments were performed using a PANalytical X-ray powder diffractometer with Cu K α radiation (40 kV, 30 mA and $\lambda = 1.5406 \text{ \AA}$) at step size of 0.026° (2°) and scan rate of $0.78^\circ/\text{min}$.

The optical reflectivity spectra $R(\omega)$ of the single crystal were measured in the frequency regions

of 70 - 12000 cm^{-1} and 25 - 150 cm^{-1} , respectively, using a Michelson-type and Martin-Puplett-type rapid-scan Fourier spectrometer (FT/IR-6100 and FARIS-1, JASCO Co, Ltd) with a feedback positioning system to maintain the overall uncertainty level with $\pm 0.3\sim 0.5\%$ over the temperature range of 8 to 300 K³⁷. To exactly obtain the absolute $R(\omega)$ values, an *in situ* Au-evaporation method was adopted³⁸. More conventional analysis of optical properties is possible from the real part of optical conductivity $\sigma_1(\omega)$, and we have derived $\sigma_1(\omega)$ from $R(\omega)$ through the Kramers-Kronig (KK) transformation. To obtain $\sigma_1(\omega)$ through the KK transformation, the reflectivity spectra were extrapolated below 25 cm^{-1} with a Hagen-Rubens function for the normal state and the form $(1 - A\omega^4)$ below the gap in the SC state. For the extrapolation above 12000 cm^{-1} , we used a constant reflectivity up to 40 eV and then used a free-electron approximation $R(\omega) \propto \omega^{-4}$.

The magnetoresistivity $\rho_{xx}(H)$ and the Hall resistivity $\rho_{xy}(H)$ were measured by the six-probe method (see Fig. S-1 in Supplementary Materials) in an Oxford superconducting magnet system. The contact lead wires (25 μm gold wire) were attached to the sample using EPO-TEK H20E epoxy. The $\rho_{xx}(H)$ and the $\rho_{xy}(H)$ were measured while sweeping the magnetic field from -5T to 5T under the transverse configuration with $B//c$ -axis and $I//ab$ -plane at various constant temperatures. The current in this measurement was $I = 15$ mA. The $\rho_{xx}(H)$ was obtained by average voltage due to positive current and negative current in each field. The ρ_{xy} was calculated using $\rho_{xy} = \frac{d}{2I} [V_{xy}(+H) - V_{xy}(-H)]$, where d is the thickness of the sample, I is the applied current, and V_{xy} is the voltage between the Hall probes.

REFERENCES

1. Ni, N., Allred, J. M., Chan, B. C. & Cava, R. J. High T_c electron doped $\text{Ca}_{10}(\text{Pt}_3\text{As}_8)(\text{Fe}_2\text{As}_2)_5$ and $\text{Ca}_{10}(\text{Pt}_4\text{As}_8)(\text{Fe}_2\text{As}_2)_5$ superconductors with skutterudite intermediary layers. *Proc. Natl. Acad. Sci. U. S. A.* **108**, E1019 (2011).
2. Löhnert, C. *et al.* Superconductivity up to 35 K in the iron platinum arsenides $(\text{CaFe}_{1-x}\text{Pt}_x\text{As})_{10}\text{Pt}_{4-y}\text{As}_8$ with layered structures. *Angew. Chem. Int. Ed.* **50**, 9195–9199 (2011).
3. Kakiya, S. *et al.* Superconductivity at 38 K in iron-based compound with platinum-arsenide layers $\text{Ca}_{10}(\text{Pt}_4\text{As}_8)(\text{Fe}_{2-x}\text{Pt}_x\text{As}_2)_5$. *J. Phys. Soc. Japan* **80**, 093704 (2011).
4. Damascelli, A., Hussain, Z. & Shen, Z. X. Angle-resolved photoemission studies of the cuprate superconductors. *Rev. Mod. Phys.* **75**, 473 (2003).
5. Sterne, P. A. & Wang, C. S. Higher T_c through metallic inter-layer coupling in $\text{Bi}_2\text{Sr}_2\text{CaCu}_2\text{O}_8$. *J. Phys. C Solid State Phys.* **21**, L949 (1988).
6. Parkin, S. S. P. *et al.* Bulk superconductivity at 125 K in $\text{Tl}_2\text{Ca}_2\text{Ba}_2\text{Cu}_3\text{O}_x$. *Phys. Rev. Lett.* **60**, 2539 (1988).
7. Gao, L. *et al.* Study of superconductivity in the Hg-Ba-Ca-Cu-O system. *Phys. C* **213**, 261 (1993).
8. Stürzer, T., Stürzer, C. & Johrendt, D. Iron arsenide superconductors $(\text{CaFeAs})_{10}\text{MnAs}_8$ with metallic interlayers (M = Pt, Pd; n = 3, 4). *Phys. Status Solidi B* **254**, 1600417 (2017).
9. Stürzer, T., Derondeau, G., Bertschler, E. M. & Johrendt, D. Superconductivity by rare earth doping in the 1038-type compounds $(\text{Ca}_{1-x}\text{RE}_x)_{10}(\text{FeAs})_{10}(\text{Pt}_3\text{As}_8)$ with RE=Y, La-Nd, Sm-Lu. *Solid State Commun.* **201**, 36–39 (2015).
10. Xiang, Z. J. *et al.* Transport properties and electronic phase diagram of single-crystalline $\text{Ca}_{10}(\text{Pt}_3\text{As}_8)((\text{Fe}_{1-x}\text{Pt}_x)_2\text{As}_2)_5$. *Phys. Rev. B* **85**, 224527 (2012).
11. Neupane, M. *et al.* Fermi-surface topology and low-lying electronic structure of the iron-based

- superconductor $\text{Ca}_{10}(\text{Pt}_3\text{As}_8)(\text{Fe}_2\text{As}_2)_5$. *Phys. Rev. B* **85**, 094510 (2012).
12. Ni, N. *et al.* Transport and thermodynamic properties of $(\text{Ca}_{1-x}\text{La}_x)_{10}(\text{Pt}_3\text{As}_8)(\text{Fe}_2\text{As}_2)_5$ superconductors. *Phys. Rev. B* **87**, 060507(R) (2013).
 13. Thirupathaiah, S. *et al.* Why T_c of $(\text{CaFeAs})_{10}\text{Pt}_{3.58}\text{As}_8$ is twice as high as $(\text{CaFe}_{0.95}\text{Pt}_{0.05}\text{As})_{10}\text{Pt}_3\text{As}_8$. *Phys. Rev. B* **88**, 140505(R) (2013).
 14. Watson, M. D. *et al.* Field-induced magnetic transitions in $\text{Ca}_{10}(\text{Pt}_3\text{As}_8)((\text{Fe}_{1-x}\text{Pt}_x)_2\text{As}_2)_5$ compounds. *Phys. Rev. B* **89**, 205136 (2014).
 15. Choi, W. J., Seo, Y. I., Ahmad, D. & Kwon, Y. S. Thermally activated flux motion in optimally electron-doped $(\text{Ca}_{0.85}\text{La}_{0.15})_{10}(\text{Pt}_3\text{As}_8)(\text{Fe}_2\text{As}_2)_5$ and $\text{Ca}_{10}(\text{Pt}_3\text{As}_8)((\text{Fe}_{0.92}\text{Pt}_{0.08})_2\text{As}_2)_5$ single crystals. *Results Phys.* **19**, 103430 (2020).
 16. Gao, P. *et al.* Pressure-Induced Superconductivity and Its Scaling with Doping-Induced Superconductivity in the Iron Pnictide with Skutterudite Intermediary Layers. *Adv. Mater.* **26**, 2346–2351 (2014).
 17. Kim, J. *et al.* Large magnetic penetration depth and thermal fluctuations in a superconducting $\text{Ca}_{10}(\text{Pt}_3\text{As}_8)[(\text{Fe}_{1-x}\text{Pt}_x)_2\text{As}_2]_5$ ($x=0.097$) single crystal. *Phys. Rev. B* **85**, 180504(R) (2012).
 18. Cho, K. *et al.* Doping-dependent superconducting gap anisotropy in the two-dimensional pnictide $\text{Ca}_{10}(\text{Pt}_3\text{As}_8)[(\text{Fe}_{1-x}\text{Pt}_x)_2\text{As}_2]_5$. *Phys. Rev. B* **85**, 020504(R) (2012).
 19. Seo, Y. I., Choi, W. J., Kimura, S. I., Bang, Y. & Kwon, Y. S. Optical properties of optimally doped single-crystal $\text{Ca}_{8.5}\text{La}_{1.5}(\text{Pt}_3\text{As}_8)(\text{Fe}_2\text{As}_2)_5$. *Phys. Rev. B* **95**, 094510 (2017).
 20. Seo, Y. I., Choi, W. J., Ahmad, D., Kimura, S. I. & Kwon, Y. S. Temperature dependence of the superconducting energy gaps in $\text{Ca}_{9.35}\text{La}_{0.65}(\text{Pt}_3\text{As}_8)(\text{Fe}_2\text{As}_2)_5$ single crystal. *Sci. Rep.* **8**, 8648 (2018).
 21. Yang, R. *et al.* Unravelling the mechanism of the semiconducting-like behavior and its relation to superconductivity in $(\text{CaFe}_{1-x}\text{Pt}_x\text{As})_{10}\text{Pt}_3\text{As}_8$. *Phys. Rev. B* **99**, 144520 (2019).

22. Wang, N. L. *et al.* High energy pseudogap and its evolution with doping in Fe-based superconductors as revealed by optical spectroscopy. *J. Phys. Condens. Matter* **24**, 294202 (2012).
23. Holland, T. J. B. & Redfern, S. A. T. UNITCELL: a nonlinear least-squares program for cell-parameter refinement and implementing regression and deletion diagnostics. *J. Appl. Crystallogr.* **30**, 84 (1997).
24. Ando, Y., Komiya, S., Segawa, K., Ono, S. & Kurita, Y. Electronic phase diagram of high- T_c Cuprate superconductors from a mapping of the In-plane resistivity curvature. *Phys. Rev. Lett.* **93**, 267001 (2004).
25. Kasahara, S. *et al.* Giant superconducting fluctuations in the compensated semimetal FeSe at the BCS-BEC crossover. *Nat. Commun.* **7**, 12843 (2016).
26. Geshkenbein, V., Ioffe, L. & Larkin, A. Superconductivity in a system with preformed pairs. *Phys. Rev. B* **55**, 3173–3180 (1997).
27. Nakajima, M. *et al.* Evolution of the optical spectrum with doping in $\text{Ba}(\text{Fe}_{1-x}\text{Co}_{1-x})_2\text{As}_2$. *Phys. Rev. B* **81**, 104528 (2010).
28. Mirri, C. *et al.* Optical conductivity of $\text{FeTe}_{1-x}\text{Se}_x$. *Supercond. Sci. Technol.* **25**, 045002 (2012).
29. Min, B. H. *et al.* Optical properties of the iron-based superconductor LiFeAs single crystal. *New J. Phys.* **15**, 073029 (2013).
30. Dai, Y. M. *et al.* Hidden T-linear scattering rate in $\text{Ba}_{0.6}\text{K}_{0.4}\text{Fe}_2\text{As}_2$ revealed by optical spectroscopy. *Phys. Rev. Lett.* **111**, 117001 (2013).
31. Wang, H. P. *et al.* Coexistence of superconductivity and density wave in $\text{Ba}_2\text{Ti}_2\text{Fe}_2\text{As}_4\text{O}$: An optical spectroscopy study. *Phys. Rev. B* **90**, 144508 (2014).
32. Yang, R. *et al.* Anomalous phonon behavior in superconducting $\text{CaKFe}_4\text{As}_4$: An optical study. *Phys. Rev. B* **95**, 064506 (2017).

33. Schafgans, A. A. *et al.* Electronic correlations and unconventional spectral weight transfer in the high-temperature pnictide $\text{BaFe}_{2-x}\text{Co}_x\text{As}_2$ superconductor using infrared spectroscopy. *Phys. Rev. Lett.* **108**, 147002 (2012).
34. Zimmermann, W., Brandt, E. H., Bauer, M., Seider, E. & Genzel, L. Optical conductivity of BCS superconductors with arbitrary purity. *Phys. C Supercond.* **183**, 99–104 (1991).
35. Seo, Y. I., Choi, W. J., Kimura, S. ichi & Kwon, Y. S. Evidence for a preformed Cooper pair model in the pseudogap spectra of a $\text{Ca}_{10}(\text{Pt}_4\text{As}_8)(\text{Fe}_2\text{As}_2)_5$ single crystal with a nodal superconducting gap. *Sci. Rep.* **9**, 3987 (2019).
36. Nakayama, K. *et al.* Superconducting gap symmetry of $\text{Ba}_{0.6}\text{K}_{0.4}\text{Fe}_2\text{As}_2$ studied by angle-resolved photoemission spectroscopy. *EPL (Europhys. Lett.)* **85**, 67002 (2009).
37. Kimura, S. Automated measurement equipment of temperature-dependent reflectivity spectra with high accuracy in the infrared and terahertz regions. *JASCO Rep.* **50**, 6 (2008). [in Japanese]
38. Kwon, Y. S. *et al.* Evidence of a pseudogap for superconducting iron-pnictide $\text{Ba}_{0.6+\delta}\text{K}_{0.4-\delta}\text{Fe}_2\text{As}_2$ single crystals from optical conductivity measurements. *New J. Phys.* **14**, 063009 (2012).

ACKNOWLEDGEMENTS

Y.S.K was supported by the National Research Foundation of Korea (NRF) grant funded by the Korea government (MSIT) (NRF-2019R1F1A1040989) and by the International Collaboration Program of Osaka University.

AUTHOR CONTRIBUTIONS

Y. S. K. designed the research. Single crystals were grown by W.J. C. and Y. I. S. X-ray diffraction, magneto-resistivity, Hall resistivity and reflectivity experiments were carried out by W.J.C. and Y.I.S. S.K. gave advice in optical experiments and helped in data analysis. The paper was written by Y.S.K, W.J.C. and Y.I.S.

COMPETING INTERESTS

The authors declare no competing interests.

Figure captions

Fig. 1 The X-ray diffraction patterns of $\text{Ca}_{8.5}\text{Na}_{1.5}(\text{Pt}_3\text{As}_8)(\text{Fe}_2\text{As}_2)_5$. Inset: the full width at half maximum (FWHM) of the (002) peak.

Fig. 2 Temperature dependence of the electrical resistivity $\rho(T)$ measured in the $\text{Ca}_{8.5}\text{Na}_{1.5}(\text{Pt}_3\text{As}_8)(\text{Fe}_2\text{As}_2)_5$ single crystal. The inset is a graph of the first derivative, $d\rho(T)/dT$, and the second derivative, $d^2\rho(T)/dT^2$, of the electrical resistivity to temperature. T_{ps} represents the temperature at which the pseudogap is observed.

Fig. 3 Reflectivity spectrum $R(\omega)$ measured at several temperatures in the $\text{Ca}_{8.5}\text{Na}_{1.5}(\text{Pt}_3\text{As}_8)(\text{Fe}_2\text{As}_2)_5$ single crystal. Inset: the reflectivity spectra $R(\omega)$ on a linear scale for a closer look at the interband transitions in the high frequency region.

Fig. 4 Optical conductivity spectra $\sigma_1(\omega)$ calculated from the reflectivity spectra $R(\omega)$ for the $\text{Ca}_{8.5}\text{Na}_{1.5}(\text{Pt}_3\text{As}_8)(\text{Fe}_2\text{As}_2)_5$ single crystal. Inset: the optical conductivity spectra $\sigma_1(\omega)$ on a linear scale for a closer look at the interband transitions in the high frequency region.

Fig. 5 Fitting results for the optical conductivity $\sigma_1(\omega)$ at $T = 150$ K using the Lorentz-Drude model: Drude responses (blue solid lines), Lorentz responses (orange dashed lines), sum of the Lorentz responses (magenta solid line).

Fig. 6 (a) The broad Drude band plasma frequency (Ω_{p1}) and the narrow Drude band plasma frequency (Ω_{p2}) obtained by fitting to the Lorentz-Drude model. **(b)** The scattering rates $1/\tau_1$ and $1/\tau_2$ for the each Drude band, **c** the d.c. conductivity $\sigma_{dc,1}$ and $\sigma_{dc,2}$ calculated by the plasma frequency and scattering rate of each band. A comparison of the sum of the two d.c. conductivities and the d.c. conductivity σ_{dc} obtained by measuring the electrical resistivity.

Fig. 7 Temperature dependence on the spectral weight (SW) normalized by the data at 300 K calculated at the cutoff frequency $\omega_c = 1000, 1500, 2000, 4000, 6000, 8000, \text{ and } 10000 \text{ cm}^{-1}$ **(a)** and $\omega_c = 50, 100, 150, 200, 500 \text{ and } 1000 \text{ cm}^{-1}$ **(b)**.

Fig. 8 (a) Temperature dependence of the carrier concentration $n(T)$ in each band evaluated by fitting the magnetic field dependence of $\sigma_{xx}(B)/\sigma_{xx}(0)$ and $\sigma_{xy}(B)$ using a two-band model. Inset: an enlarged plot for a closer look at the carrier concentration $n(T)$ of the broad Drude band. **(b)** Temperature dependence of the mobility $\mu(T)$ in each band evaluated by fitting the magnetic field dependence of $\sigma_{xx}(B)/\sigma_{xx}(0)$ and $\sigma_{xy}(B)$ using the two-band model.

Fig. 9 Fitting of the excitation spectrum only by the superconducting gap open at 8 K using a generalized Mattis-Bardeen equation.

Table

Table. 1. Fitting parameters $P_k = \sqrt{S_k Z_0 / 2\pi}$, ω_{Lk} and $1/\tau_{Lk}$ in the Lorentzian components for interband transitions obtained by fitting optical conductivity at 150 K using the L-D model, where S_k is the oscillator strength and Z_0 is the impedance of free space.

	Lorentz Osc. 1	Lorentz Osc. 2	Lorentz Osc. 3	Lorentz Osc. 4
P_k (cm ⁻¹)	1333.8	1905.7	5055.7	9363.7
ω_{Lk} (cm ⁻¹)	266.0	394.3	725.3	1240.0
$1/\tau_{Lk}$ (cm ⁻¹)	81.6	282.8	383.2	1240.0

	Lorentz Osc. 5	Lorentz Osc. 6	Lorentz Osc. 7	Lorentz Osc. 8
P_k (cm ⁻¹)	126118.6	26986.2	20440.9	42279.9
ω_{Lk} (cm ⁻¹)	2383.3	5099.6	7225.9	12951.7
$1/\tau_{Lk}$ (cm ⁻¹)	2244.2	5257.7	6283.3	12000.0

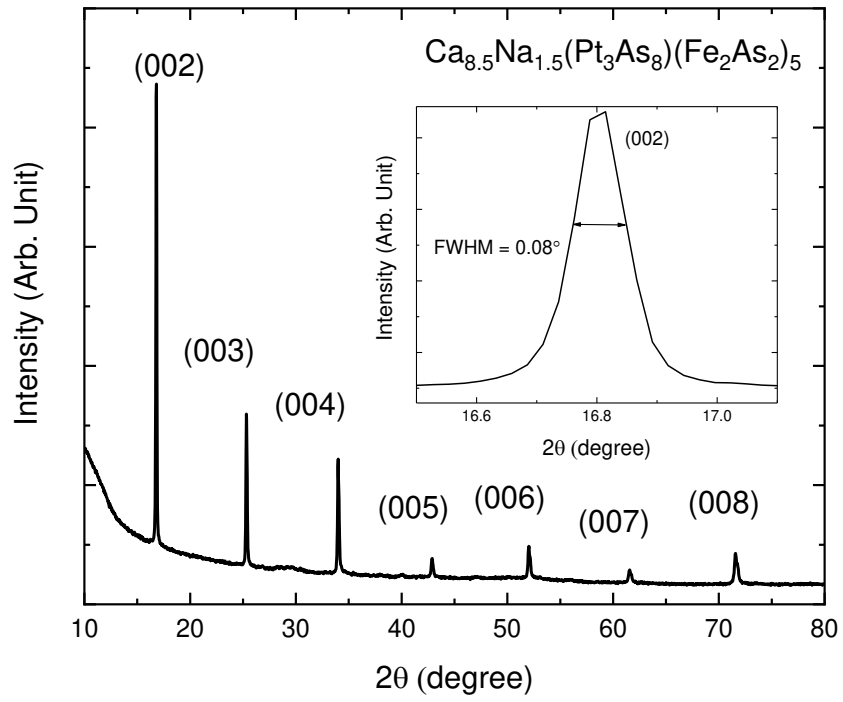


Fig. 1

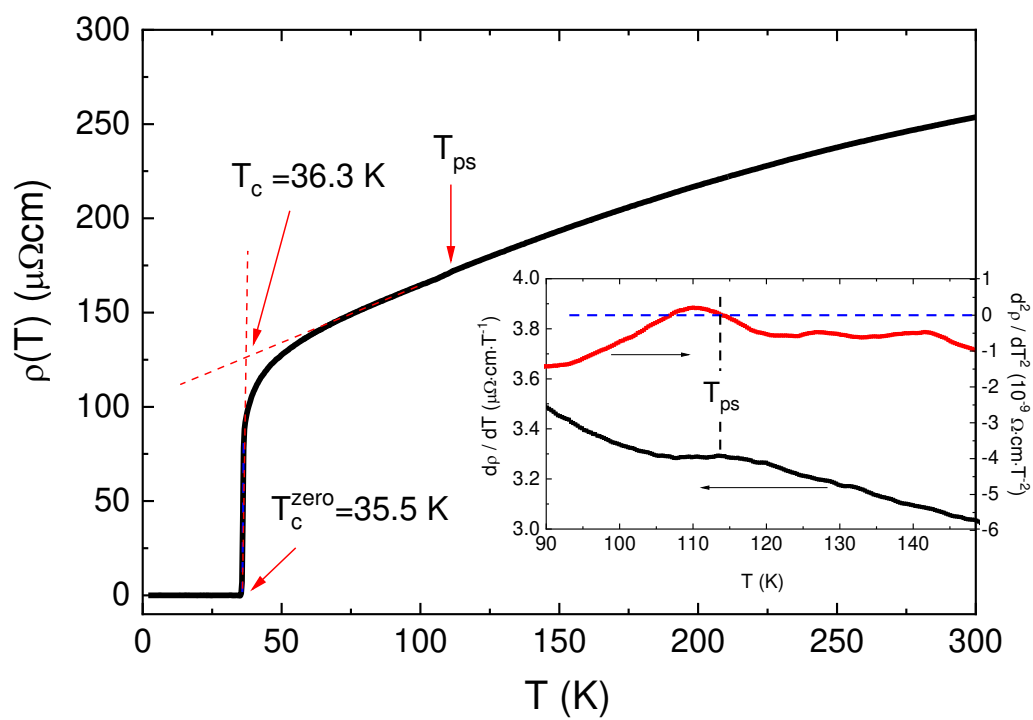


Fig. 2

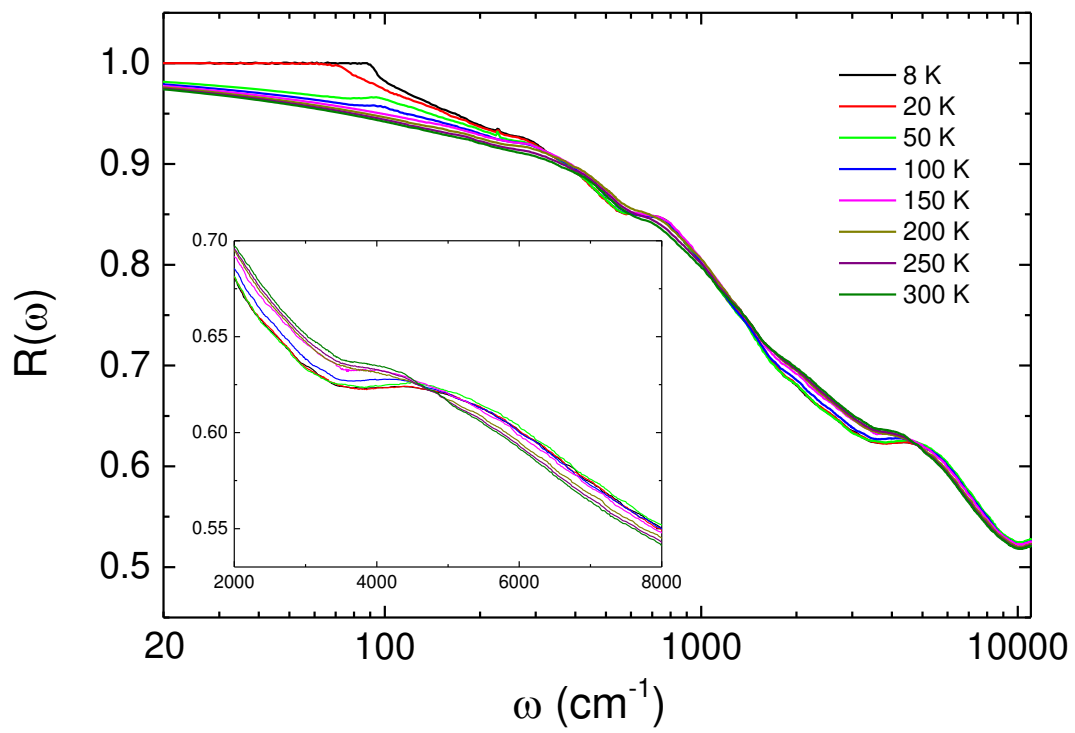


Fig. 3

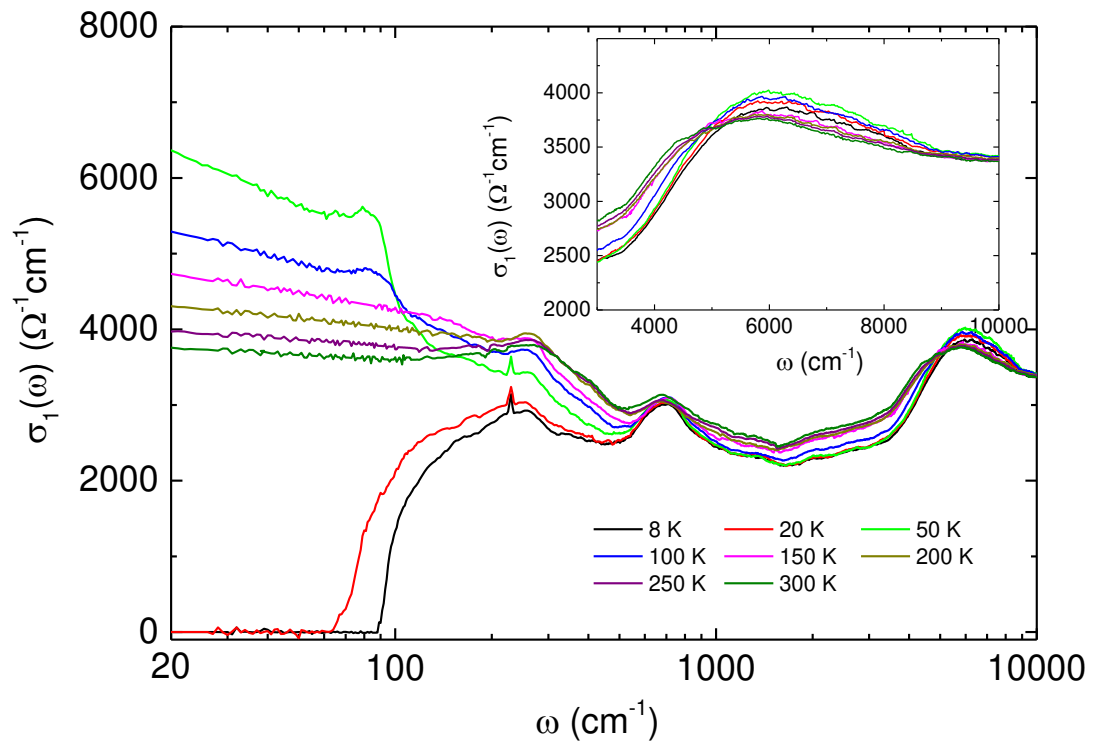


Fig. 4

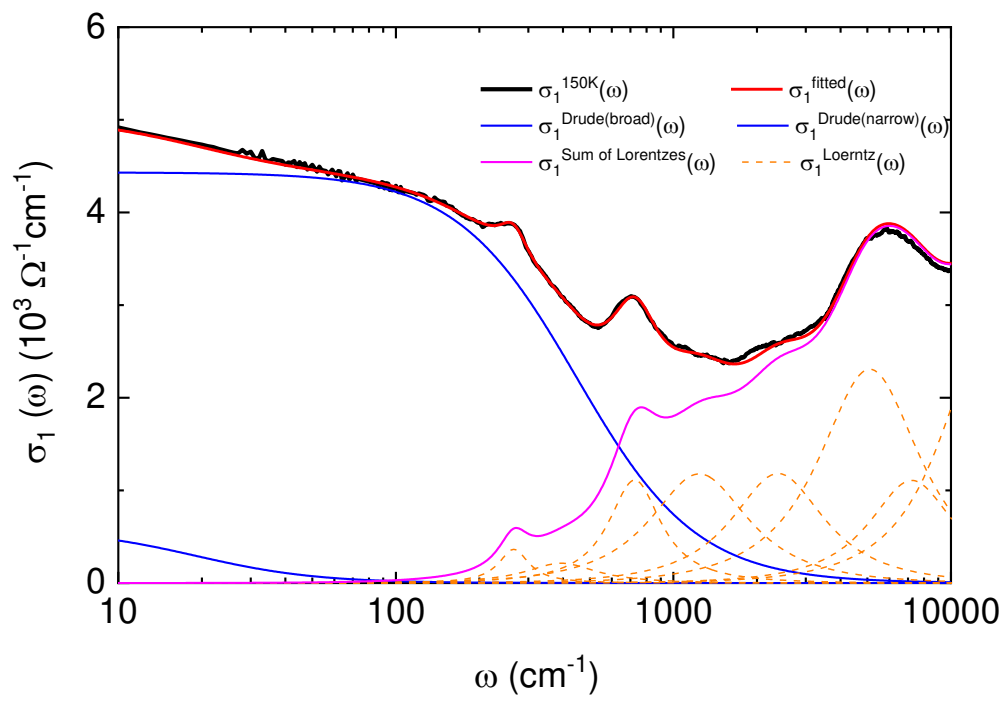


Fig. 5

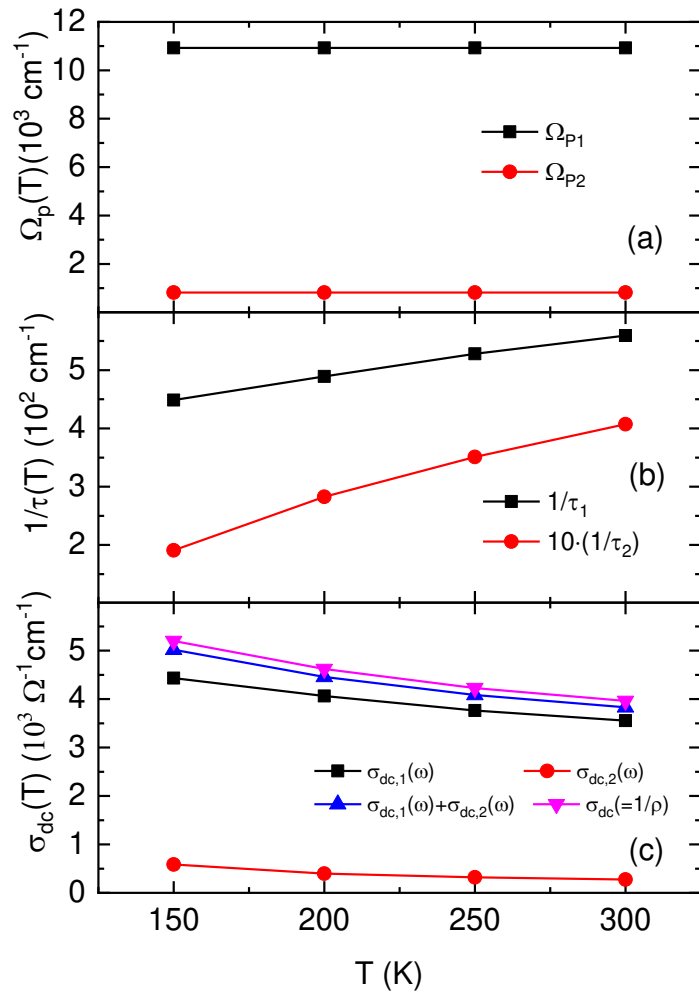


Fig. 6

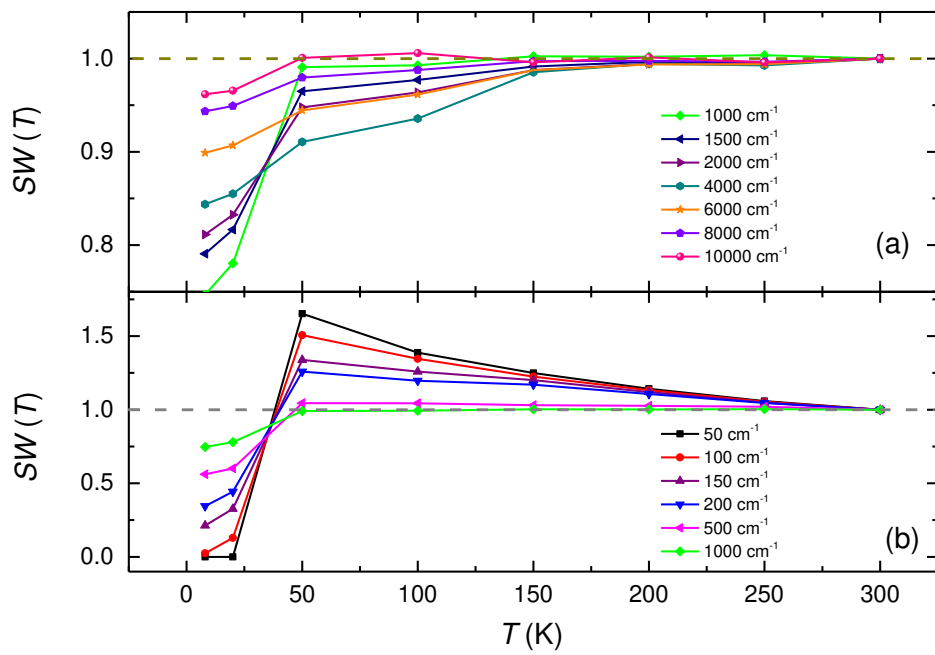


Fig. 7

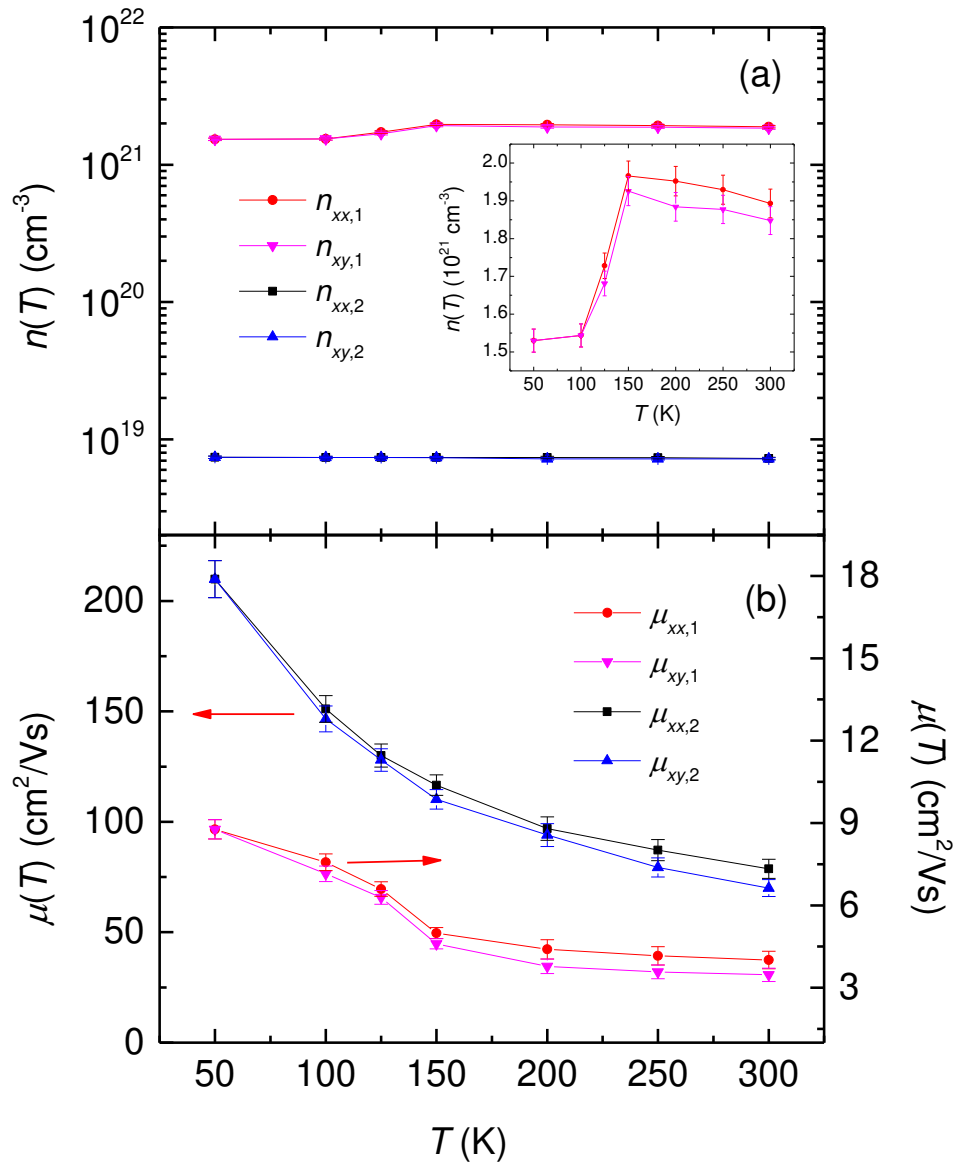


Fig. 8

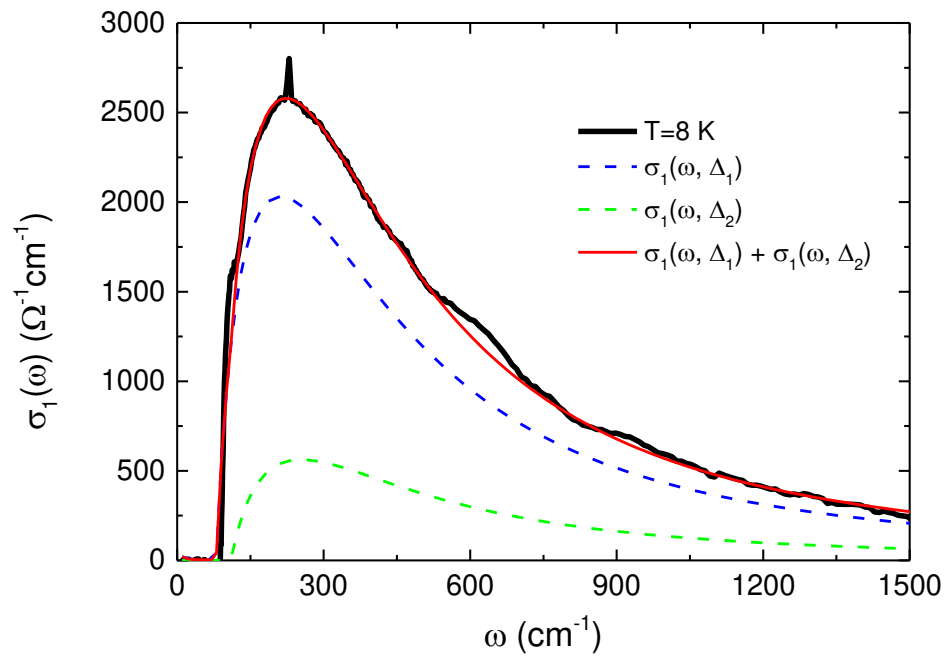


Fig. 9

Figures

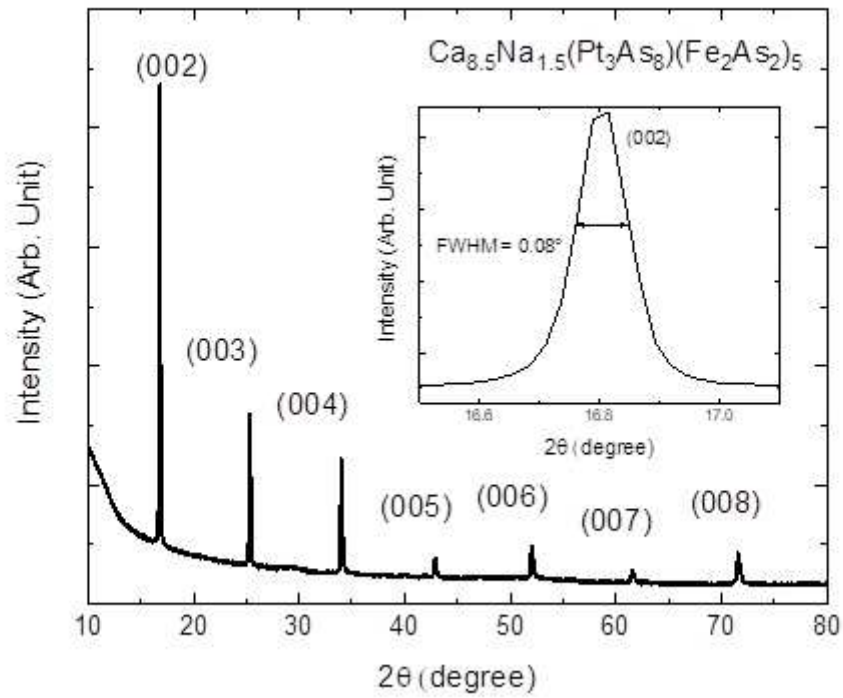


Figure 1

The X-ray diffraction patterns of $\text{Ca}_{8.5}\text{Na}_{1.5}(\text{Pt}_3\text{As}_8)(\text{Fe}_2\text{As}_2)_5$. Inset: the full width at half maximum (FWHM) of the (002) peak.

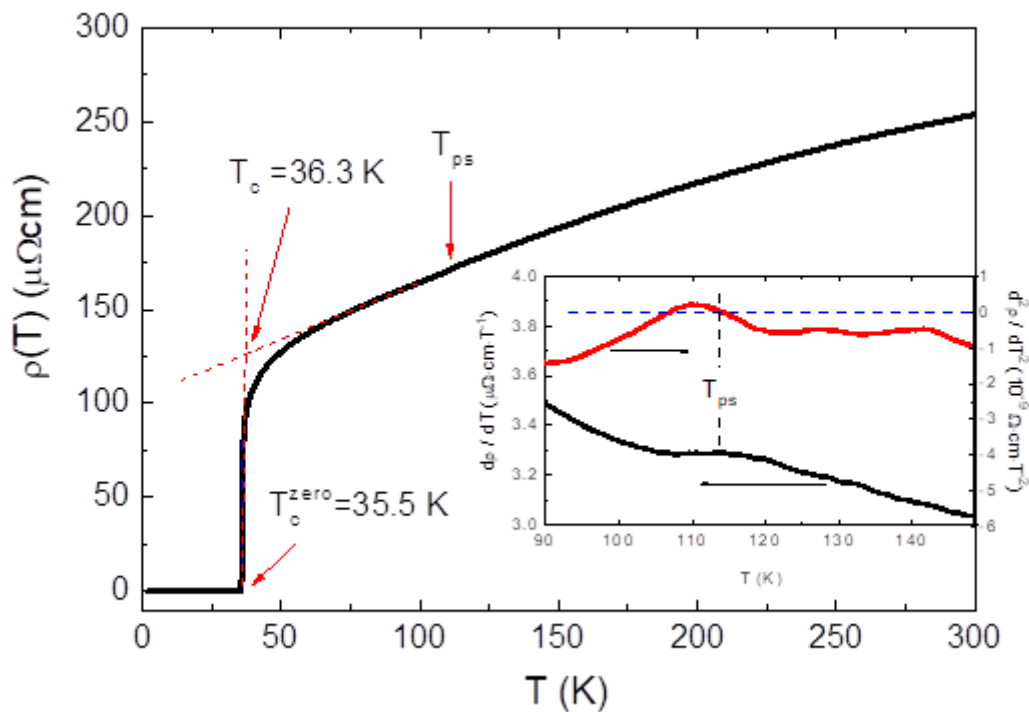


Figure 2

Temperature dependence of the electrical resistivity $\rho(T)$ measured in the $\text{Ca}_{8.5}\text{Na}_{1.5}(\text{Pt}_3\text{As}_8)(\text{Fe}_2\text{As}_2)_5$ single crystal. The inset is a graph of the first derivative, $d\rho(T)/dT$, and the second derivative, $d^2\rho(T)/dT^2$, of the electrical resistivity to temperature. T_{ps} represents the temperature at which the pseudogap is observed.

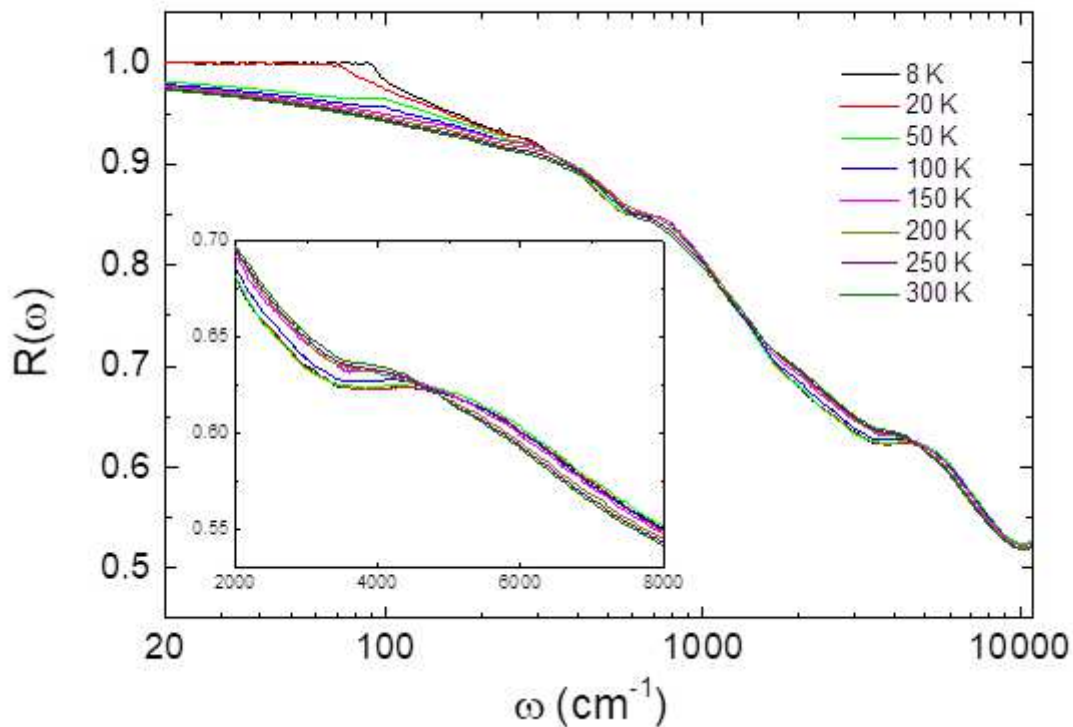


Figure 3

Reflectivity spectrum $R(\omega)$ measured at several temperatures in the $\text{Ca}_{8.5}\text{Na}_{1.5}(\text{Pt}_3\text{As}_8)(\text{Fe}_2\text{As}_2)_5$ single crystal. Inset: the reflectivity spectra $R(\omega)$ on a linear scale for a closer look at the interband transitions in the high frequency region.

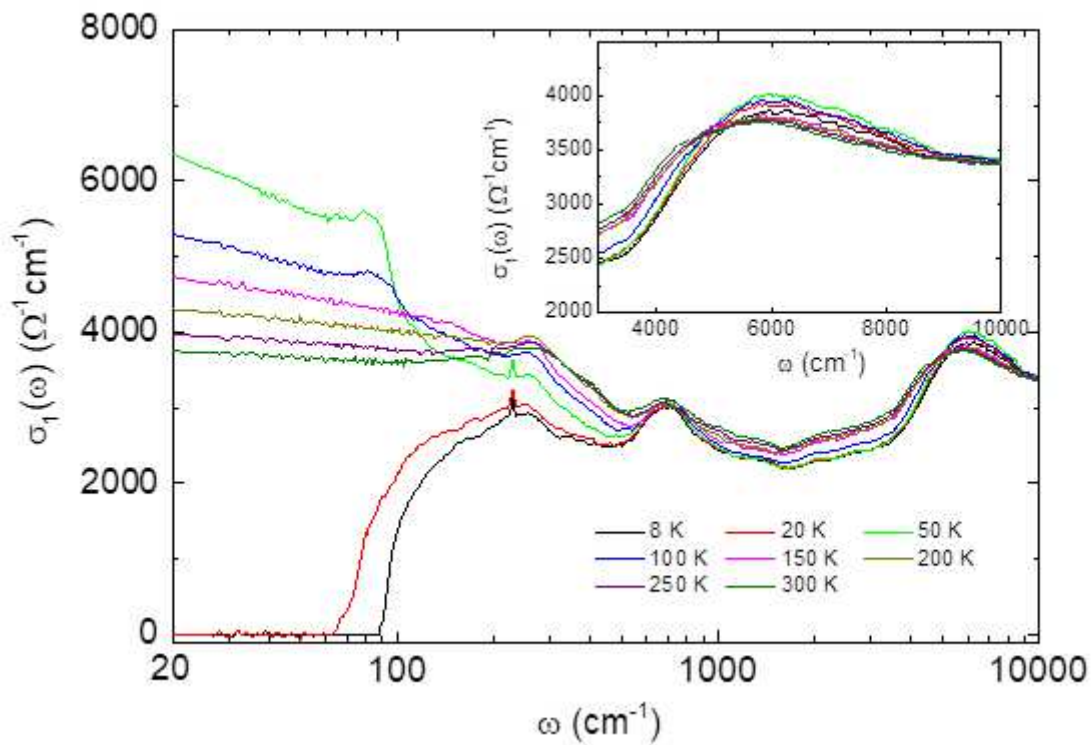


Figure 4

Optical conductivity spectra $\sigma_1(\omega)$ calculated from the reflectivity spectra $R(\omega)$ for the $\text{Ca}_{8.5}\text{Na}_{1.5}(\text{Pt}_3\text{As}_8)(\text{Fe}_2\text{As}_2)_5$ single crystal. Inset: the optical conductivity spectra $\sigma_1(\omega)$ on a linear scale for a closer look at the interband transitions in the high frequency region.

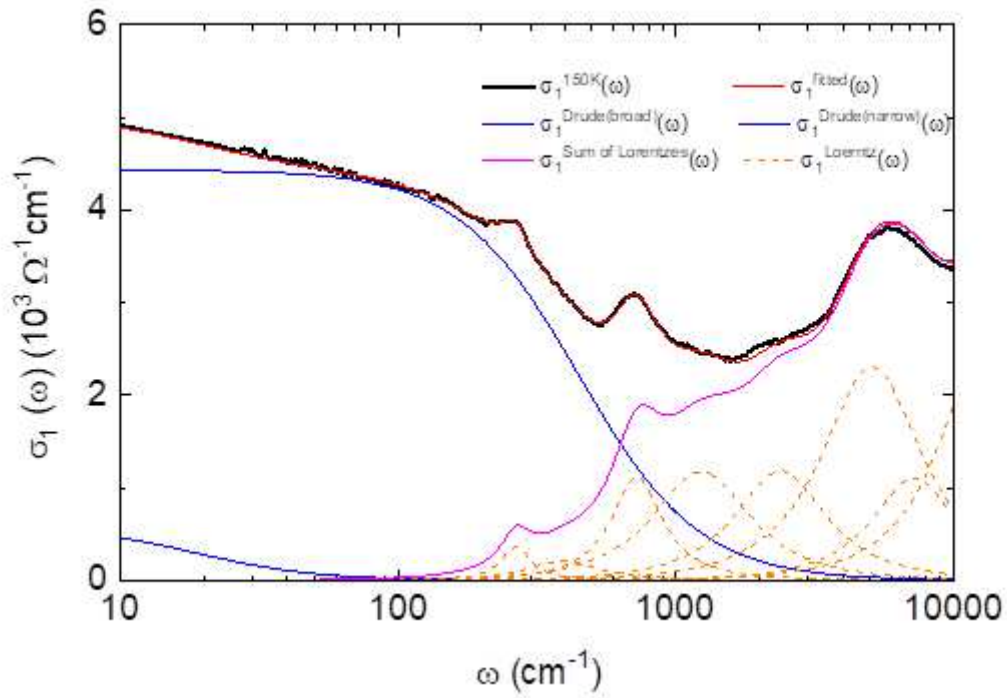


Figure 5

Fitting results for the optical conductivity $\sigma_1(\omega)$ at $T = 150 \text{ K}$ using the Lorentz-Drude model: Drude responses (blue solid lines), Lorentz responses (orange dashed lines), sum of the Lorentz responses (magenta solid line).

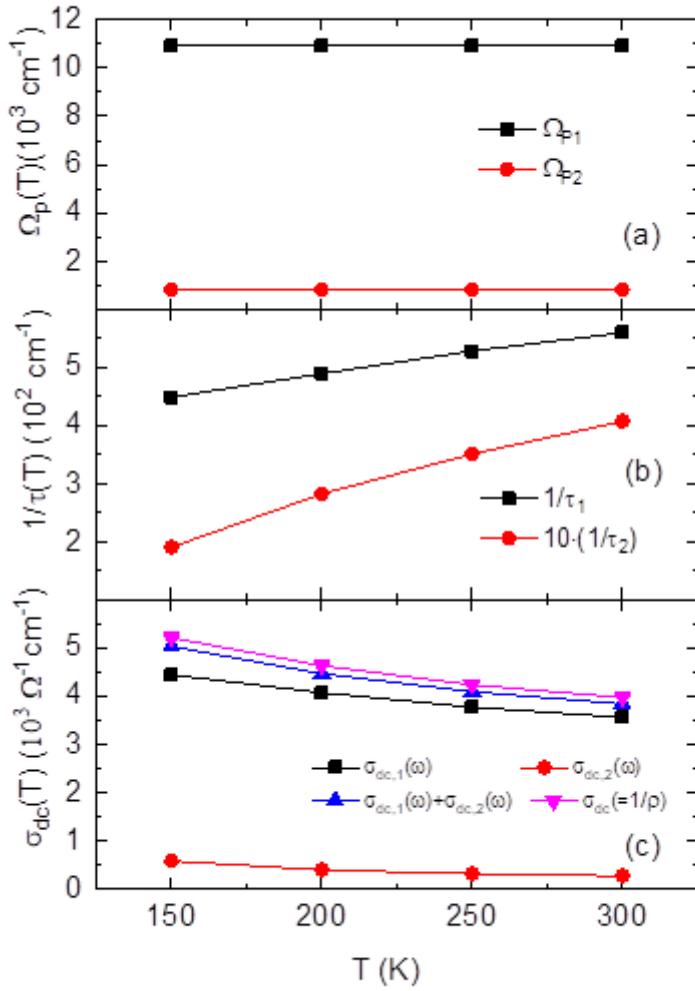


Figure 6

(a) The broad Drude band plasma frequency (Ω_{P1}) and the narrow Drude band plasma frequency (Ω_{P2}) obtained by fitting to the Lorentz-Drude model. (b) The scattering rates $1/\tau_1$ and $1/\tau_2$ for the each Drude band, c the d.c. conductivity $\sigma_{dc,1}$ and $\sigma_{dc,2}$ calculated by the plasma frequency and scattering rate of each band. A comparison of the sum of the two d.c. conductivities and the d.c. conductivity σ_{dc} obtained by measuring the electrical resistivity.

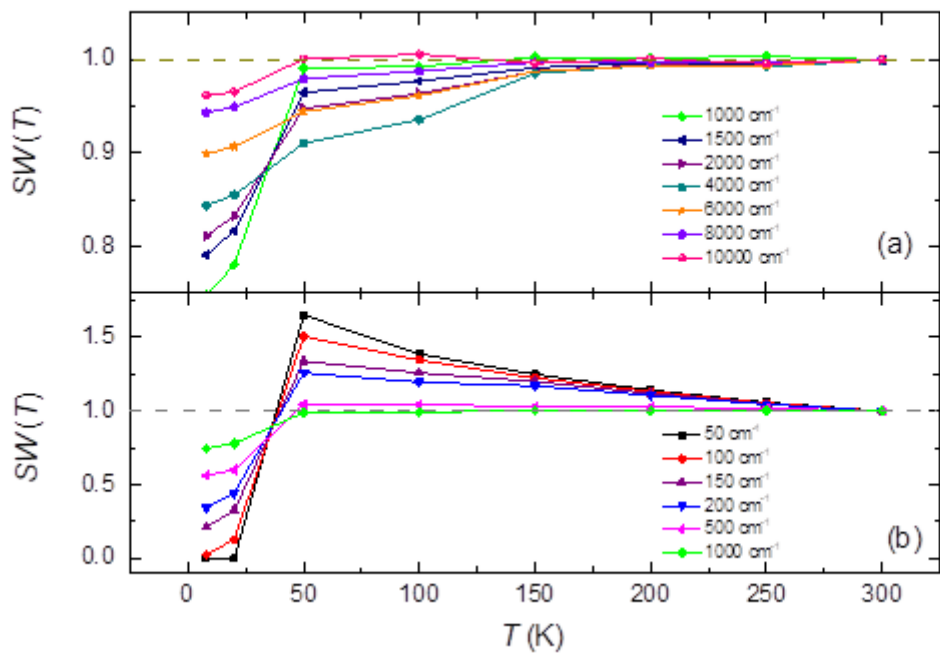


Figure 7

Temperature dependence on the spectral weight (SW) normalized by the data at 300 K calculated at the cutoff frequency $\omega_c = 1000, 1500, 2000, 4000, 6000, 8000, \text{ and } 10000$ cm⁻¹ (a) and $\omega_c = 50, 100, 150, 200, 500$ and 1000 cm⁻¹ (b).

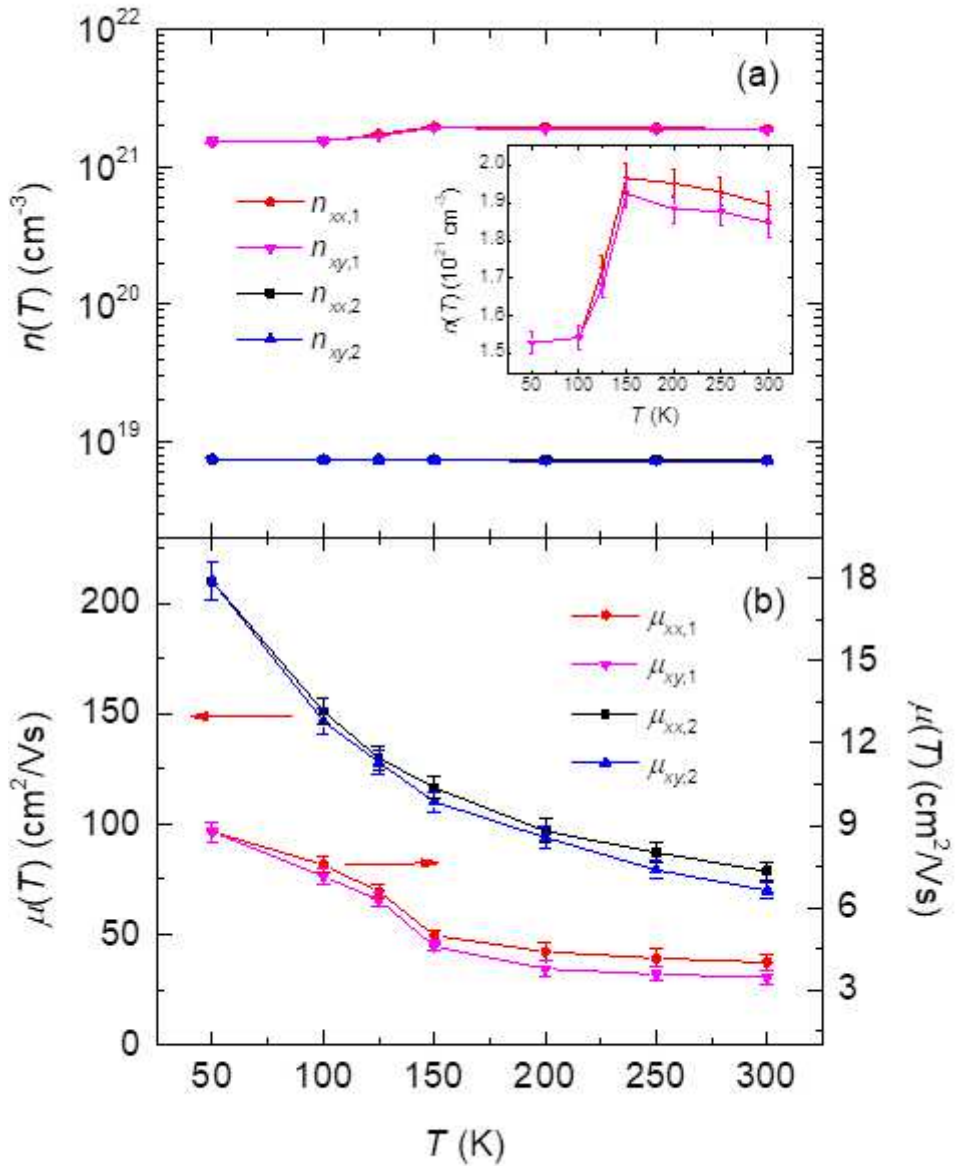


Figure 8

(a) Temperature dependence of the carrier concentration $n(T)$ in each band evaluated by fitting the magnetic field dependence of $\sigma_{xx}(B)/\sigma_{xx}(0)$ and $\sigma_{xy}(B)$ using a two-band model. Inset: an enlarged plot for a closer look at the carrier concentration $n(T)$ of the broad Drude band. (b) Temperature dependence of the mobility $\mu(T)$ in each band evaluated by fitting the magnetic field dependence of $\sigma_{xx}(B)/\sigma_{xx}(0)$ and $\sigma_{xy}(B)$ using the two-band model.

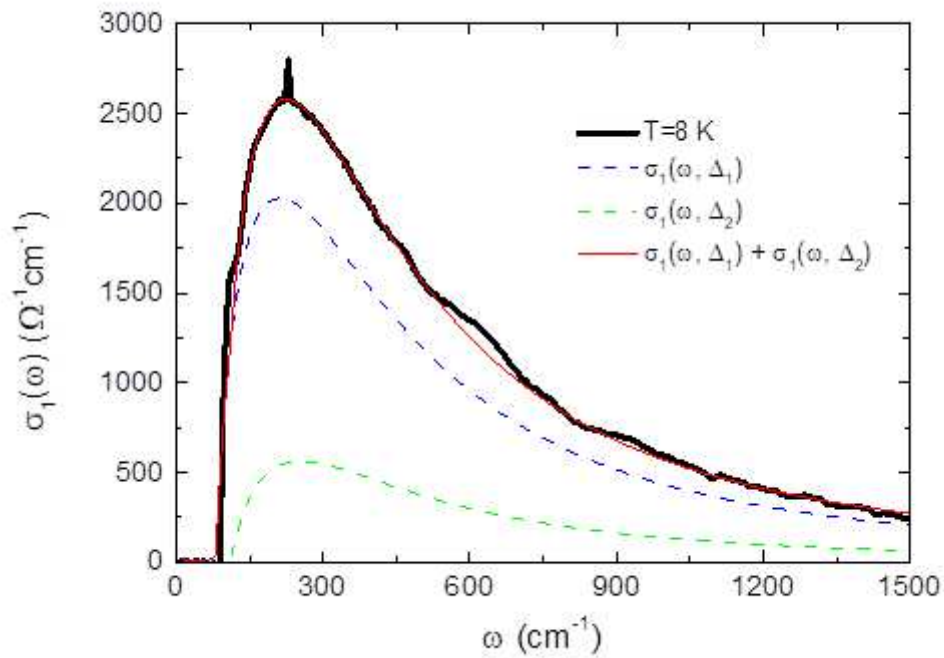


Figure 9

Fitting of the excitation spectrum only by the superconducting gap open at 8 K using a generalized Mattis-Bardeen equation.

Supplementary Files

This is a list of supplementary files associated with this preprint. Click to download.

- [SupplementaryInformation.pdf](#)